PHYSICAL REVIEW B **98**, 155308 (2018)

Conductivity and transparency limits of Sb-doped SnO_2 grown by molecular beam epitaxy

R. F. Martinez-Gazoni,[1,2,*] M. W. Allen,[2,3] and R. J. Reeves[1,2]
[1] *School of Physical and Chemical Sciences, University of Canterbury, Christchurch 8140, New Zealand*
[2] *MacDiarmid Institute for Advanced Materials and Nanotechnology, Wellington 6012, New Zealand*
[3] *Department of Electrical and Computer Engineering, University of Canterbury, Christchurch 8140, New Zealand*

(Received 22 March 2018; revised manuscript received 18 September 2018; published 11 October 2018)

Ultraviolet (UV)/visible/infrared (IR) transmission spectroscopy, Hall effect measurements and synchrotron x-ray photoelectron spectroscopy were used to determine the limits of Sb doping on the electrical and optical properties of single crystal SnO_2 (101) films grown by molecular beam epitaxy. The resistivity (ρ) and carrier density (n) of these Sb:SnO_2 films could be varied by more than seven orders of magnitude, covering the insulating, semiconducting, and semimetallic regimes, by adjusting the Sb fraction in the incident metal flux from 0 to 3.0 at. %, corresponding to a Sb incorporation of up to 8×10^{20} atoms/cm^3. A maximum conductivity limit of $\rho \approx 6 \times 10^{-4}\,\Omega\,\text{cm}$ and $n \approx 4 \times 10^{20}\,\text{cm}^{-3}$ was determined at approximately 3×10^{20} Sb atoms/cm^3, after which an increase in ρ (and decrease in n) with increasing Sb flux was observed, most likely due to charge compensation arising from the preferential formation of Sb^{3+} acceptors. The limits for the coexistence of transparency and electrical conductivity were found to be governed by a Burstein-Moss shift of the optical gap (E_{opt}) in the UV spectrum and a much larger blue shift of the free-carrier adsorption edge in the IR region due to an increasing plasma frequency (ω_p), with both effects scaling with the carrier concentration of the Sb:SnO_2 films. Despite these effects, the transparency window in the visible region was almost unaffected, with more than 90% transmission in the 350–1500 nm range for 150-nm-thick Sb:SnO_2 films at the conductivity limit. The density of states reduced effective mass and the conductivity effective electron mass were determined from the variation of ω_p and E_{opt} with n, resulting in values of $(0.46 \pm 0.12)\,m_e$ and $(0.31 \pm 0.10)\,m_e$, with the difference consistent with a shrinkage of the fundamental gap due to many-body interactions. Finally, the correlation between the changes in E_{opt} and n with increasing Sb incorporation was used to provide an estimate for the charge neutrality level of SnO_2 of +0.49 eV above the conduction band minimum.

DOI: 10.1103/PhysRevB.98.155308

I. INTRODUCTION

Wide band gap transparent conducting oxides (TCOs) that combine both high transparency and strong electrical conductivity are the subject of significant research interest due to their increasing use in solar cell technology, touch screens, optical displays, and transparent electronic devices [1–4]. Among these, stannic oxide (SnO_2) is a promising earth-abundant transparent binary oxide, with an unusually high chemical stability and low toxicity, which is already found in solar cells and gas sensing devices [5,6]. SnO_2 crystallizes in the rutile structure with a tetragonal unit cell of the group $P4_2/mnm$ and lattice constants $a = b = 4.7374$ Å and $c = 3.1864$ Å [7]. While insulating in its pure stoichiometric form, SnO_2 usually possesses a significant unintentional n-type conductivity [7] that is generally attributed to nonstoichiometric effects, although there is significant debate as to the identity of the defects responsible. Central to this debate is a disagreement over the nature of oxygen vacancies (V_O) as either deep or shallow donors in SnO_2, due to the different band gap corrections used in the first principles calculation of defect level states [8–12]. It has been proposed that interstitial tin (Sn_i) forms a spontaneously ionized donor level 203 meV above the conduction band minimum and directly promotes the formation of oxygen vacancies, an effect assisted by the multivalence nature of Sn (i.e., Sn^{4+} and Sn^{2+}). However, other theoretical studies have questioned the role of Sn_i as a significant donor, due to its high formation energy and low migration barrier [9,12,13]. It has also been shown that hydrogen exclusively acts as a donor in SnO_2 (and many other TCOs), in particular forming a shallow donor level inside an oxygen vacancy (H_O) where it is stabilized by multicentered bonding with the nearest-neighbor cations [9]. King *et al.* [13,14] have proposed that the unintentional n-type conductivity of SnO_2 and other TCOs, such as ZnO, In_2O_3, and CdO can be explained by the fact that their charge neutrality level (CNL) are located above the conduction band minimum (CBM), which tends to favor the formation of donor-like native defect, localized impurity, and surface states. This is in contrast to most other semiconductors in which the CNL lies within the fundamental gap.

Transport measurements of unintentionally doped (UID) poly- and single-crystalline SnO_2 films typically show carrier concentrations (n), mobilities (μ), and resistivities (ρ) in the range of 10^{17}–$10^{20}\,\text{cm}^{-3}$, 10–$100\,\text{cm}^2/\text{Vs}$ and 10^{-2}–$10^{-3}\,\Omega\,\text{cm}$, respectively [15–17]. Further increases in the conductivity of SnO_2 have usually been achieved by intentionally doping the host material with Sb and F in the 1% to 25% range [16–20]. Co, Mo, and Ni have also been

---

[*] rodrigo.martinezgazoni@canterbury.ac.nz

2469-9950/2018/98(15)/155308(10)

used as donors but to a lesser extent [15,21,22]. Like all TCOs, ambipolar doping is problematic, although Al, Ga, and In have been investigated as potential acceptor candidates [4,23].

Theoretical calculations [24,25] are known to significantly underestimate the fundamental band gap of SnO_2, which is *a posteriori* corrected to a typical value of 3.6 eV [8,9,24,25]. Experimental studies on the optical properties of SnO_2 have reported direct optical band gaps in the range of 3.5–4.2 eV [21,26–29]. The wide range of reported values has been attributed to variations in crystalline quality, stoichiometry, and impurity content of different SnO_2 materials, and also to the diversity of experimental and analytical methods employed for its determination [26–29]. Sabino *et al.* [30] have recently shown that in oxides such as SnO_2, in which selection rules prevent transitions from the valence band maximum to the conduction band minimum, intense illumination can promote weak transitions from near the top of the valence band, leading to optical band gap values close to the fundamental gap. However, under low and moderate illumination conditions only strong transitions are accessible, resulting in a widening of the optical band gap of up to ~0.7 eV in the case of SnO_2 [30].

Despite its potential for transparent electronics and sensing applications [21,31–33], the study of the fundamental nature of SnO_2 has been hindered by the lack of commercially available single crystals and by the defective nature of UID material produced by most deposition techniques, which typically results in carrier concentrations in the $10^{18}-10^{20}\,\mathrm{cm}^{-3}$ range [7,17,34,35]. The reproducible growth of high structural quality, single crystal material is required to explore the optical and electrical limits of SnO_2. Previous work [23,36] concerning the growth of single crystal SnO_2 films by plasma assisted molecular beam epitaxy (PAMBE) explored the conditions that produced single phase material, with a particular focus on maximizing the growth rate. These studies produced UID epitaxial SnO_2 (101) thick films (of up to 1500 nm) with n as low as $3 \times 10^{17}\,\mathrm{cm}^{-3}$ and μ up to $15\,\mathrm{cm}^2/\mathrm{Vs}$ (26 nm single layer) and $100\,\mathrm{cm}^2/\mathrm{Vs}$ (1570 nm including a very thick buffer layer). While not electrically intrinsic in nature, these films allowed an exploration of the semiconducting regime of the material, a region not previously accessible. Subsequent Sb-doping during PAMBE growth produced a monotonic decrease in resistivity with doping level suggesting that all the Sb atoms were incorporated as ionized donors. Despite the high carrier concentrations obtained for Sb-doped SnO_2 films (up to $2.8 \times 10^{20}\,\mathrm{cm}^{-3}$), these studies did not establish the Sb:doping limit for PAMBE SnO_2 [17,37] or explore the effect of Sb doping on the transparency window of SnO_2.

In this work, we have optimized the PAMBE growth of SnO_2 (101) films to obtain intrinsic, highly resistivity material with $\rho > 1\,\mathrm{k}\,\Omega$ cm and $n < 10^{14}\,\mathrm{cm}^{-3}$, with high bulk crystallinity and atomically abrupt step-terraced surfaces. These films represent the highest quality intrinsic, single crystalline SnO_2 (101) films reported so far and are therefore ideal springboards to explore the ultimate limits of the material. These intrinsic SnO_2 (101) films were used to investigate the effects of Sb doping on the electrical and optical properties of SnO_2 and explore the limits for the coexistence of high transparency and conductivity in this technologically important TCO.

II. EXPERIMENTAL METHODS

Intrinsic SnO_2 films of thicknesses up to 600 nm were grown by PAMBE in a Thermionics ultrahigh vacuum chamber with a base pressure lower than 4×10^{-9} Torr. Double-sided polished r-plane sapphire substrates ([1–102], MTI corp.) were used to induce heteroepitaxial growth in the (101) direction with minimal lattice mismatch. A high temperature effusion cell (e-science Inc.) operated from 900 to 1200 °C was used to produce a metallic beam of Sn (99.999%, Lesker Company Ltd.), while an Oxford Applied Research HD25 RF plasma source operated at 200W was used to generate an oxygen plasma beam at 3.5×10^{-5} Torr that produced oxygen-rich conditions, as indicated by Sn/O flux calculations and previous literature reports [23]. At the limits of our x-ray diffraction (XRD) and x-ray photoelectron spectroscopy (XPS) studies, these conditions produced stoichiometric SnO_2 (101) films, with no other phases observed. An e-science LT Titan effusion cell was used as the Sb source (99.999%, Kamis Inc.) to explore the doping limits of Sb:SnO_2 films. Source and dopant atomic fluxes were calibrated with a MacVac quartz crystal microbalance that measured the Sn/Sb atomic flux ratio incident on the substrate. Sb atomic concentrations were determined by calibrated secondary ion mass spectroscopy (SIMS) measurements conducted in a Cameca IMS-6f ion microprobe system using a positive Caesium beam. A Staib RH20 reflection high energy electron diffraction (RHEED) system operating at 20 kV provided real-time assessment of the epitaxial growth mode, lattice matching, and surface crystallinity.

Substrate preparation involved sonication in trichloroethylene, acetone, and methanol followed by indium-bonding to a molybdenum mounting block that was then loaded into the molecular beam epitaxy (MBE) chamber. *In situ* preparation of the substrate surface involved a 30-min bake at 800 °C, followed by a 30-min oxygen plasma treatment at 800 °C. This produced a pristine, epi-ready surface, evidenced by sharp RHEED patterns with distinct Kikuchi lines. No further RHEED improvement was observed after an additional 800 °C annealing step, as used elsewhere [38–40], and atomic force microscopy (AFM) and XRD studies of films grown with and without this step were undistinguishable from each other. A total of 46 UID SnO_2 films obtained at different substrate temperatures, cell temperatures, and film thicknesses were used to explore the growth modes involved, optimize film quality, and assess the origin of the electrical conductivity in UID SnO_2 films.

The surface morphology of the films was studied *ex situ* in a Raith 150 scanning electron microscope (SEM) at typical accelerating voltages of 10 kV and in a Veeco Dimension 3100 AFM operated in tapping mode. The thicknesses of the resulting SnO_2 films ranging from 20 to 600 nm were measured using a high resolution JEOL JSM-7000F SEM, while specular x-ray reflectivity (XRR) techniques were adopted for sub-20 nm films. A Bruker D8 diffractometer equipped with a Co radiation source was used to investigate the crystal orientation and the quality of the films, via θ–2θ and ω scans in the Bragg-Brentano configuration, respectively. XPS studies conducted at the soft x-ray (SXR) beamline of the Australian Synchrotron confirmed the stoichiometry of the intrinsic SnO_2

films and the presence of Sb in the doped material. The optical properties of the SnO_2 films were explored in the ultraviolet (UV), visible, near-infrared (IR) and mid-far IR parts of the spectrum with an Agilent Cary 6000i spectrophotometer, a Bruker Tensor 37 Fourier-transform infrared (FTIR) system and a Bruker Vertex 70 FTIR system, covering a wide spectral range from 200 to 16 000 nm.

The electrical properties of the films were investigated using an EGK HEM-2000 Hall effect measurement system and an Agilent B1500A semiconductor device analyzer. Resistivity measurements were performed in the van der Pauw configuration and the carrier type, carrier concentration, and mobility at room temperature were obtained through Hall measurements conducted under a 0.51 T magnetic field.

III. RESULTS AND DISCUSSION

A. Intrinsic UID SnO_2 (101) films

An extensive study of the effect of growth conditions on the structural, optical, and electrical properties of PAMBE SnO_2 was initially carried out to establish the optimal conditions for producing the highest quality intrinsic SnO_2 (101) films (as described in detail in the supplementary information [41]). These optimized conditions involved substrate and Sn cell temperatures of 800 and 1075 °C, respectively, and low growth rates of less than 1 nm/min, resulting in ∼100-nm films characterized by streaky RHEED patterns both during and after growth, XRD ω-FWHM of $(0.6 \pm 0.1)^\circ$, and atomically smooth surfaces with abrupt step-terraces (see Fig. 1).

Figure 2 presents the UV-visible transmission spectra of a typical 100-nm-thick UID SnO_2 (101) film grown using the optimized conditions, showing more than 93% transmission across the entire visible range. The inset shows the corresponding Tauc plot from which an optical band gap of $(4.03 \pm 0.03\,\mathrm{eV})$ was extracted. Synchrotron XPS was used to assess the near-surface stoichiometry of the intrinsic SnO_2 (101) films. While the Sn 3d emission has been used to distinguish SnO from SnO_2 [42], this analysis can be susceptible to misinterpretation because the relatively small difference in binding energy between Sn^{2+} and Sn^{4+} ($<$0.7 eV) can be obscured by screening effects that vary with the carrier concentration of the material [43,44]. Conventional analysis of O 1s and Sn 3d core level spectra is therefore not considered to be effective in distinguishing SnO_2 from SnO [45,46], and instead the valence band (VB) spectra was used to identify the predominant phase [45–49]. A well-established method for distinguishing SnO_2 from SnO involves studying the energetic separation between the Sn 4d 5/2 emission and the lowest binding energy (BE) peak in the VB region [7]. The energy difference between these features in SnO is known to be close to 23.7 eV, more than 2 eV larger than in SnO_2 (21.1 eV) [7,45,46,49]. In addition, a Sn^{2+} related shoulder at BE between 2 and 3 eV is also associated with the presence of a SnO phase [46,49]. Conversely, the lack of this shoulder and the presence of a distinct emission with a BE close to 10 eV (assigned to Sn 5s-O 2p bonding states) is a spectral signature of SnO_2 [46–49]. The 2–3 eV shoulder has also been attributed to Sn-Sn defects [42], although our studies show that the annealing of similar SnO_2 films removes surface oxygen, forming a SnO-like surface that is accompanied by the emergence of this spectral feature. This shoulder also disappears upon reoxidation of the surface in ambient conditions. Our interpretation is also in agreement with previous studies on SnO films, which showed the appearance of the 2–3eV emission as the topmost SnO_2 surface layer was removed [46].

Figure 3 shows a typical XPS spectrum of the intrinsic SnO_2 (101) films in which the energy difference between the Sn 4d 5/2 emission and the lowest BE VB peak (∼21.2 eV) is characteristic of SnO_2. In addition, the absence of the 2–3 eV shoulder associated with SnO and the strong emission close to 10 eV indicates the presence of a pure SnO_2 phase.

The improvement in crystal quality and surface roughness achieved in the optimization of the intrinsic UID SnO_2 (101) PAMBE films (see supplementary information [41]) was accompanied by a significant increase in electrical resistivity, consistent with a defect origin (Sn_i and V_O or H_O) of the unintentional n-type conductivity of SnO_2. Significantly, the resistivity of the fully-optimized UID SnO_2 (101) films was beyond the measurements limit of $\rho > 1\ \mathrm{k\Omega\,cm}$ regardless of thickness, indicating intrinsic-like material quality. In addition, the resistivity of the partially optimized UID SnO_2 (101) films (grown at a Sn cell temperature of 1100 °C instead of 1075 °C) was found to increase with film thickness, as shown in Fig. 4. RHEED, AFM, and XRD/XRR studies comparing the coherent and the total thickness (see supplementary information [41]) indicated a high concentration of structural defects within the first five atomic layers of the film and a much lower concentration in subsequent layers once the lattice mismatch between the substrate and film had been accommodated and epitaxial growth established. The large increase in resistivity with film thickness is therefore a consequence of the highly localized nature of the defects responsible for the electrical conductivity in these films.

B. Sb-doped SnO_2 (101) films–limit of conductivity

A wide range of 150-nm-thick, Sb-doped, SnO_2 (101) PAMBE films (Sb:SnO_2) were grown to investigate the electrical and transparency limits of Sb:SnO_2 as a TCO. The films were deposited using the previously established optimized growth conditions, i.e., a substrate temperature of 800 °C, Sn and Sb fluxes coevaporated at temperatures of 1075 °C and 180–360 °C, respectively, and a 200-W oxygen plasma beam at a partial pressure of 3.5×10^{-5} Torr. These conditions allowed the Sb fraction in the total incident metallic flux to be varied between 0 and 3.0 at. %, while maintaining the single phase growth of high quality Sb:SnO_2 (101) material as indicated by RHEED and XRD measurements. Figure 5(a) shows the effect of Sb doping on the resistivity at 300 K of the resulting Sb:SnO_2 films, where the efficient incorporation of Sb donors is evident by a more than four orders of magnitude decrease in resistivity for Sb concentrations of less than $4 \times 10^{19}\ \mathrm{atoms/cm^3}$.

Figure 5(a) also shows that as the Sb concentration increases beyond $\sim 3 \times 10^{19}\ \mathrm{atoms/cm^3}$, the rate of decrease in resistivity significantly slows and a turning point is reached at a Sb concentration of $\sim 3 \times 10^{20}\ \mathrm{atoms/cm^3}$, corresponding to a minimum resistivity of $\rho \approx 6 \times 10^{-4}\ \Omega\,\mathrm{cm}$. Any further

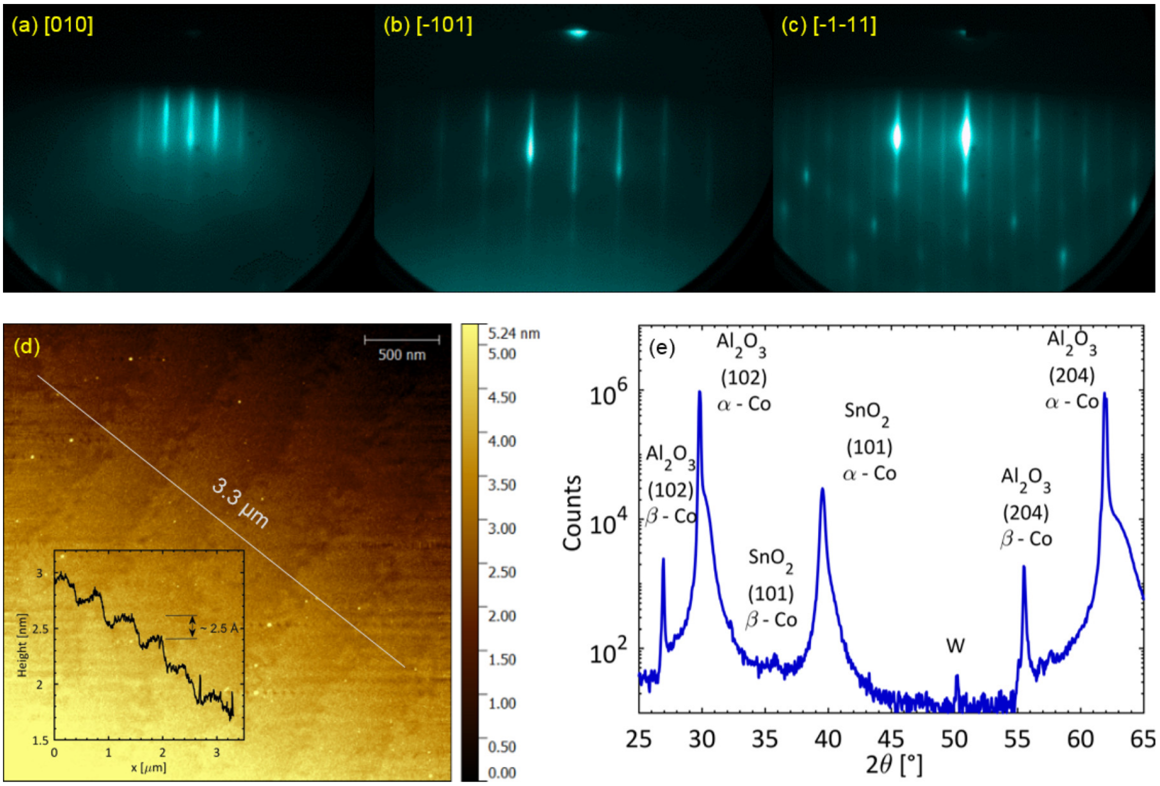

FIG. 1. (a)–(c) RHEED diffraction patterns of a typical optimized 100-nm-thick UID SnO_2 (101) film grown using substrate and Sn cell temperatures of 800 and 1075 °C, respectively. Multiple orientations were probed by rotating the sample in the azimuth angle, all exhibiting well-defined streaks indicative of a highly crystalline surface. (d) Corresponding AFM image of the surface of the film exhibiting wide terraces defined by atomic steps, as shown in the height profile (inset). (e) XRD θ–2θ scans indicating the presence of a single phase (101) SnO_2 film. The broadening observed in the substrate peaks is associated with Bremsstrahlung radiation, which does not affect the position of the peaks nor their FWHM.

increase in the Sb fraction resulted in a gradual increase in resistivity, indicating that a maximum Sb doping limit for the increase of n-type conductivity in Sb:SnO_2 had been reached. This limit can also be seen in the dependence of carrier concentration on Sb fraction, shown in Fig. 5(b), where a maximum value of $n \approx 4 \times 10^{20}\ \text{cm}^{-3}$ occurs at the same $\sim 3 \times 10^{20}\ \text{atoms/cm}^3$ Sb concentration as for the resistivity minimum.

An almost unity relationship was observed between the carrier concentration and Sb atomic concentration in the 3×10^{19} to $3 \times 10^{20}\ \text{atoms/cm}^3$ range [Fig. 5(b)] that indicates a Sb^{5+} donor efficiency of close to 100% over this

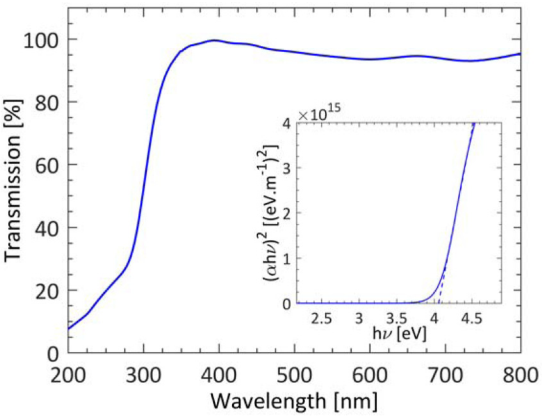

FIG. 2. UV-visible transmission spectra of a typical optimized 100-nm-thick UID SnO_2 (101) film with the inset showing the Tauc plot used to determine the optical band gap.

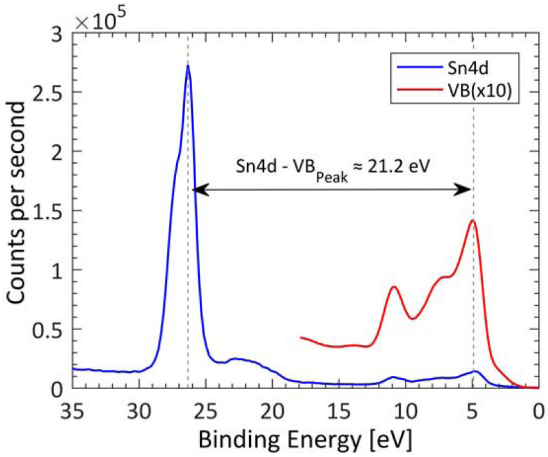

FIG. 3. Room temperature XPS spectra of the Sn 4d 5/2 (blue) and valence band (red) region of a typical intrinsic SnO_2 (101) film. The energy difference between the Sn 4d 5/2 peak and the VB lowest BE peak is in agreement with that reported for pure SnO_2.

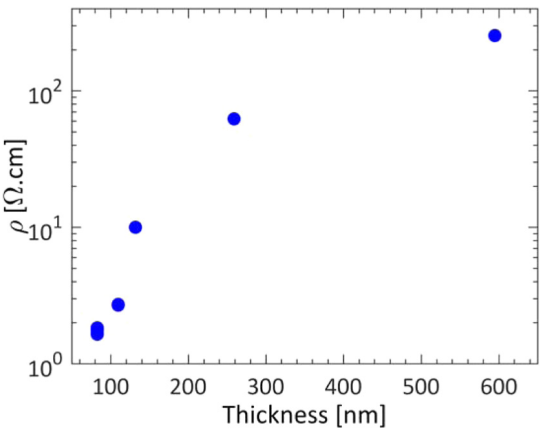

FIG. 4. Electrical resistivity of undoped SnO_2 (101) films as a function of film thickness measured using the Van der Pauw method at 300 K. Note: these films were only partially optimized, being grown at a Sn cell 1100 °C instead of 1075 °C. This was necessary because the resistivity of the fully optimized films at all thickness was above the $\rho > 1\,k\Omega$ cm measurement limit of the semiconductor parameter analyzer.

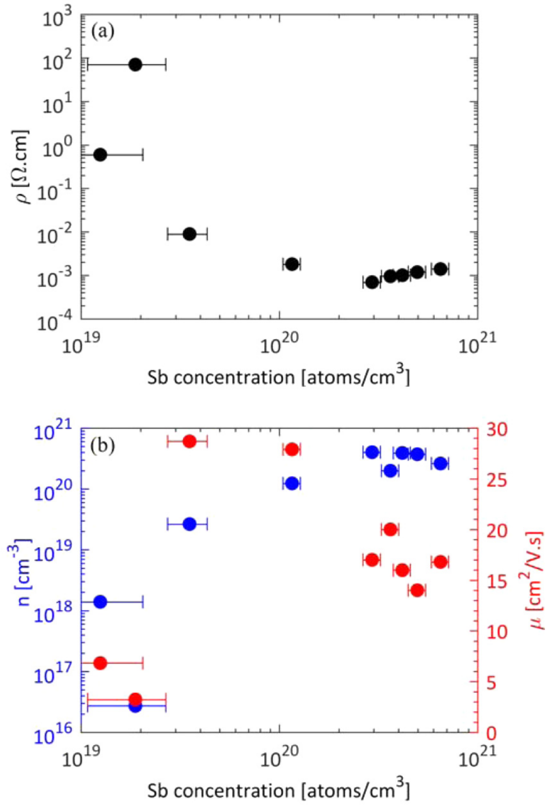

FIG. 5. (a) Resistivity (black), (b) carrier concentration (blue) and carrier mobility (red) of 150-nm-thick $Sb:SnO_2$ (101) films grown by PAMBE as a function of the atomic Sb concentration. Note: the carrier concentration of the intrinsic UID film at an Sb flux = 0% was less than 10^{14} cm^{-3}.

range. This is in agreement with previous studies by White *et al.* [17] and Feneberg *et al.* [50] on Sb-doped SnO_2 films grown by PAMBE under similar conditions. However, these studies only explored a maximum Sb concentration of 2.8×10^{20} atoms/cm^3 and therefore the effects of Sb doping beyond this point cannot be compared. The significantly higher doping levels achieved in this work accessed an additional regime characterized by a significant decrease in donor efficiency resulting in a maximum conductivity limit. This indicates the emergence of a charge compensation mechanism, possibly due to the presence of Sb in the +3 valence state at higher doping levels. High-resolution XRD (HRXRD) and photoluminescence (PL) studies on epitaxial and polycrystalline films have reported Sb^{5+}/Sb^{3+} compensation occurring at doping levels in the 1–10% wt. range, which is consistent with the results obtained herein [27,34,51].

Our interpretation of the decrease in carrier concentration that limits the conductivity of $Sb:SnO_2$ films is due to a competition between Sb^{5+} and Sb^{3+} as the substituting species. At lower Sb concentrations, the doping mechanism favors Sb^{5+} ions substituting Sn^{4+} ions in the SnO_2 lattice, donating electrons to the conduction band and thus increasing the carrier concentration and decreasing the resistivity of the material (i.e., the region up to $\sim 3 \times 10^{20}$ Sb atoms/cm^3 in Fig. 5). As the Sb concentration increases, the formation energy for Sb^{3+} substitution of Sn^{4+} ions decreases [35,52,53]. In this valence state, Sb^{3+} on Sn^{4+} sites produces an acceptor concentration that reduces the number of carriers available for conduction and increases the resistivity of the sample (i.e., the 3×10^{20} to 8×10^{20} Sb atoms/cm^3 region in Fig. 5). While the presence of this charge compensation model has been proposed in SnO_2 polycrystalline films [27,34,51], the results presented here are evidence of the mechanism occurring in high quality single crystal SnO_2.

Within this model, the observed conductivity limit at an Sb concentration of $\sim 3 \times 10^{20}$ atoms/cm^3 corresponds to the position of the Fermi level for which the formation energy of donor-like Sb^{5+} and acceptor-like Sb^{3+} substituents are the same. The limiting n observed in this work is in close agreement with the maximum values reported for other Sb-doped epitaxial SnO_2 films (Table I), thus supporting the proposed model for the maximum limit for Sb doping in SnO_2. Interestingly, the conductivity limit of $n \approx 4 \times 10^{20}$ cm^{-3} is the same as that observed by Swallow *et al.* [20] in a recent study of self-compensation in F-doped SnO_2, suggesting that conductivity limit in SnO_2 films may be the same for different dopants.

Swallow *et al.* [20] used XPS analysis to explore a similar compensation mechanism in heavily doped F-SnO_2 films, with interstitial fluorine (F_i) acting as single-charged acceptors that compensate substitutional fluorine (F_O) donors, thus limiting the n-conductivity of the films. Unfortunately, such analysis was not possible in our Sb-doped films because the binding energies of $Sb3d_{5/2}$ emission associated with the Sb^{5+} and Sb^{3+} oxidation states are relatively close to each other and also directly overlap the O 1s spectral region, thus making any deconvolution of these states unreliable [54]. In addition, the O 1s emission also exhibits considerable spectral broadening due to adsorbed OH and H_2O species which further complicates any attempt of deconvolution [54,55]. Analysis of other Sb-related XPS peaks (such as the $Sb3d_{3/2}$ emission) was not possible due to their weak intensities and high signal-to-noise ratios, even with the use of Synchrotron

TABLE I. Maximum n and corresponding μ and ρ of epitaxial Sb:SnO$_2$ films.

Method	Orientation	Dopant	n [$\times 10^{20}$ cm^{-3}]	μ [cm^2/Vs]	ρ [$\times 10^{-3}$ Ω cm]	Reference
MOCVD[a]	(101)	Sb	2.5	18	1.3	[52]
MBE	(101)	Sb	2.6	36	0.7	[17]
MBE	(101)	Sb	4.0	17	0.6	This work
MBE	(100)	Sb	4.1	4.5	3.4	[37]
MOCVD	(100)	Sb	5.3	12	0.9	[35]
APCVD[b]	-	F	4.0	40	0.4	[20]

[a] Metal-organic chemical vapor deposition.

[b] Atmospheric-pressure CVD.

radiation. However, Terrier *et al.* [56] were successful in deconvoluting the Sb^{3+} and Sb^{5+} contributions to the Sb3d$_{3/2}$ peak in highly doped SnO$_2$ films grown by sol-gel, and they showed the emergence of the Sb^{3+} contribution as the Sb concentration increased beyond 4%, until it became the dominant component at 22%. This dominant Sb^{3+}/Sn^{4+} substitution at high Sb concentration was accompanied by a plateau in the (so far decreasing) resistivity, in agreement with the results presented here and with the compensation model proposed.

While no significant degradation in the structural quality of the 150-nm Sb:SnO$_2$ films with increasing Sb fraction was observed using *in situ* RHEED and *ex situ* XRD, the incorporation of Sb atoms had a significant effect on the carrier mobility, as shown in Fig. 5(b). Peak carrier mobilities of 29 cm^2/V s were obtained at Sb concentration of 3.5×10^{19} atoms/cm^{-3}. As the incorporation of Sb increases (in both Sb^{5+} and Sb^{3+} forms), increased ionized impurity scattering reduces the mobility to the 13–19 cm^2/V s range. Higher mobilities approaching 100 cm^2/V s have been reported for much thicker (~1500 nm) Sb:SnO$_2$ PAMBE films that also involved a thick UID SnO$_2$ buffer layer whose contribution was analytically separated.

The highly resistive nature of the intrinsic PAMBE SnO$_2$ material grown here allowed carrier concentration control via Sb doping (without the need for a buffer layer) over $<10^{14}$–10^{20} cm^{-3} range encompassing the insulating, semiconducting, and semimetallic transport regimes.

C. Sb-doped SnO$_2$ (101) films–limit of transparency

Figure 6 shows the effect of Sb doping on the UV-visible-IR transparency of the 150-nm-thick Sb:SnO$_2$ (101) PAMBE films. More than 95% transparency across the entire 350–10 000 nm range was observed in films with carrier concentrations of up to 10^{18} cm^{-3} (corresponding to Sb concentration of up to 2×10^{19} atoms/cm^{-3}). Further increase in carrier concentration significantly reduced the transparency of the films in the mid-IR region, with a more than tenfold reduction in the size of the IR transparency window for Sb:SnO$_2$ (101) films at the carrier concentration limit of $n \approx 4 \times 10^{20}$ cm^{-3}.

In the mid/far-IR region the transparency loss is associated with free-carrier oscillations, characterized by the plasma cut-off frequency ω_p, and by its effect on the permittivity $\boldsymbol{\varepsilon}$ of the medium. In the Drude model these effects are given by

$$\omega_p{}^2 = \frac{e^2}{\varepsilon_0 \varepsilon_\infty m_c^*} n, \tag{1}$$

$$\boldsymbol{\varepsilon} = \varepsilon_{\mathrm{Re}} + i\varepsilon_{\mathrm{Im}} = \left(1 - \frac{\omega_p^2}{\omega^2}\right) + i\left(\frac{\varepsilon_\infty \omega_p^2}{\omega^3 \tau}\right), \tag{2}$$

where e is the electron charge, n is the carrier concentration, ε_∞, ε_0 are the high frequency and free space permittivity respectively, m_c^* is the conductivity effective mass, ω is the incident wave frequency, and τ is the relaxation time between collisions. As the carrier concentration increases, $\boldsymbol{\varepsilon}$ becomes imaginary for progressively shorter wavelengths [Eq. (2)] producing a blue-shift of the IR adsorption edge. However, it is clear from Fig. 6 that while the shift of the plasma edge to lower wavelengths resulted in a significant reduction of the IR transparency window, it had little effect on the transparency of the Sb:SnO$_2$ films in the visible spectrum. Even at the carrier concentration limit of $n \approx 4 \times 10^{20}$ cm^{-3} the Sb:SnO$_2$ films maintained more than 90% transparency across the 350–1500 nm range.

In the UV region (see Fig. 6) the band edge is noticeably blue shifted as n increases. This is due to the Burstein-Moss (BM) effect whereby the increasing carrier concentration leads to the filling of lowest conduction band states. This

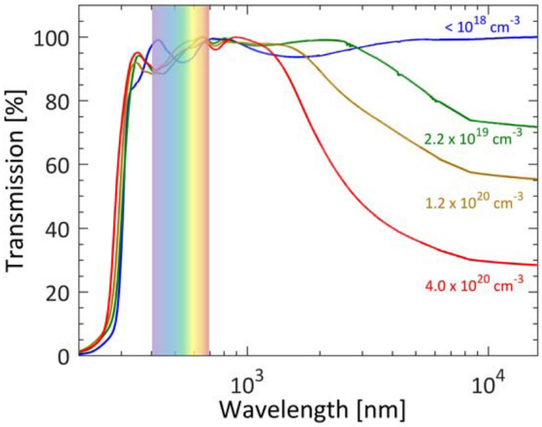

FIG. 6. UV-visible-IR spectra of 150-nm-thick Sb:SnO$_2$ (101) films with increasing carrier concentration.

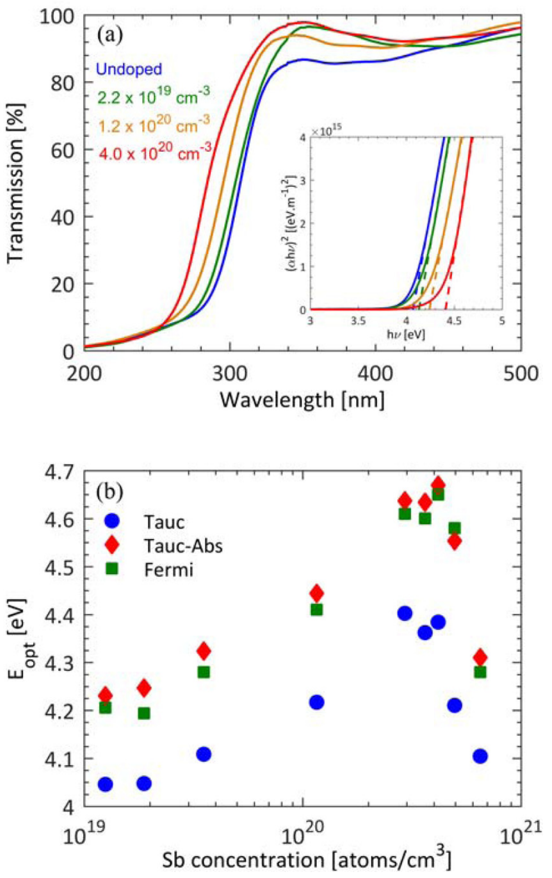

FIG. 7. (a) UV-visible spectra of Sb:SnO_2 (101) films with increasing doping level. Inset: Tauc plot used for extracting the optical band gap, exhibiting a strong BM shift. (b) Optical band gap obtained from UV-visible studies, indicating the filling of the conduction band as the Sb concentration increases and suggesting the emergence of the Sb^{5+}/Sb^{3+} charge compensation mechanism for Sb doping levels beyond 3×10^{20} atoms/cm^3. Circles, diamond, and square markers correspond to the values extracted from Tauc plots, combined Tauc and absorption coefficient extrapolation, and Fermi-Dirac fits of the absorption edge.

raises the Fermi level into the conduction band, increasing the energy of the lowest energy band-to-band optical transitions due to Pauli blocking. Fig. 7(a) shows the transmission of typical Sb:SnO_2 films in the UV-visible region in greater detail, in which the BM shift with increasing n can be more clearly seen.

The corresponding Tauc plots used to extract E_{opt} are shown in the inset of Fig. 7(a). While obtaining the optical band gap using Tauc plots is only strictly valid in the case of nondegenerate semiconductors under the parabolic band approximation, this method has been widely used in the literature for a wide range of doping levels. We have, therefore, included Tauc plots in our analysis to allow a comparison of our results with previous studies. However, alternative methods for obtaining the optical gap from transmission or absorption spectra have been proposed by Dolgonos *et al.* [57] using time-dependent perturbation theory. These methods involve the use of combined Tauc and absorption coefficient spectra plots or direct Fermi-Dirac distribution fitting of the absorption spectra. Both methods were also used in this work with the results shown in Fig. 7(b). Although the absolute values of E_{opt} vary between methods (i.e., being ~150 meV higher using the two methods of Dolgonos *et al.*) the relative trends and BM shifts are almost identical. Figure 7(b) shows the dependence of E_{opt} with Sb concentration, which is characterized by a rapid increase of (0.49 ± 0.08) eV as the Sb fraction is increased up to $\sim 3 \times 10^{20}$ atoms/cm^3, followed by a decrease in E_{opt} for Sb fractions beyond this value. This dependence mirrors the relationship between the carrier concentration and Sb fraction shown in Fig. 7(b) that also reaches a maximum at a Sb concentration of $\sim 3 \times 10^{20}$ atoms/cm^3.

As expected, the maximum BM shift in E_{opt} of 0.49 eV coincides with the maximum conductivity limit $n \approx 4 \times 10^{20}$ cm^{-3} of the Sb:SnO_2 films. Within the CNL model, this value can be used to provide an estimate for the CNL of SnO_2, of $E_{\text{CNL}} = E_{\text{CBM}} + (0.49 \pm 0.08)$eV. Within the model, the CNL provides a guide to the position of E_{F} at which the formation energies of donor-like and acceptor-like forms of certain localized impurity and native defects are likely to be the same [13,14]. This would be expected to occur near the conductivity limit assuming the formation energies of both the dopant and native defect states involved follow similar trends or if the concentration of native defects is negligible compared to that of the donor (Sb^{5+}) and acceptor-like (Sb^{3+}) states associated with Sb doping. The very good crystalline quality of both the undoped and Sb-doped films up to the conductivity limit as observed in both XRD and RHEED measurements suggest that the latter may indeed be the case in the films studied here. Despite these assumptions, the experimentally derived CNL value for SnO_2 is very close to the theoretical value of $E_{\text{C}} + 0.5$ eV reported by Falabretti and Robertson [58,59]. The discrepancy may be in part due to many-body effects caused by the high free electron density at the conductivity limit, which can result in band-gap narrowing and cause the energetic separation between the CNL and the CBM to be underestimated [60,61]. Vasheghani Farahani explored the surface-state charge density and surface band bending in Sb-doped PAMBE SnO_2 (101) films as a function of carrier concentration showing that both decreased as E_{F} increases towards the CNL [62]. However, the maximum Sb-doping level (carrier concentration) of their films was 3.5×10^{19} atoms/cm^3 $(2.6 \times 10^{19}$ cm$^{-3})$ and consequently they still exhibited significant downward surface band bending consistent with $E_{\text{F}} < E_{\text{CNL}}$.

Using a free-electron-like parabolic dispersion for the conduction band minimum of SnO_2, the dependence of BM shift on carrier concentration can be expressed as [19,63]

$$E_{\text{opt}} = E_{\text{g}} + \frac{\hbar^2 (3\pi^2)^{\frac{2}{3}}}{2m_{\text{d}}^*} n^{\frac{2}{3}}. \tag{3}$$

Equations (1) and (3) were used to fit the observed variations of the plasma frequency and the optical band gap of the Sb:SnO_2 films with n, respectively, and thereby determine values for the conductivity effective mass m_{c}^* and the density of states reduced effective mass m_{d}^*. Figure 8 presents the results of these fits, from which values of m_{c}^* $(0.31 \pm 0.10)\, m_e$ and m_{d}^* $(0.46 \pm 0.12)\, m_e$ were obtained.

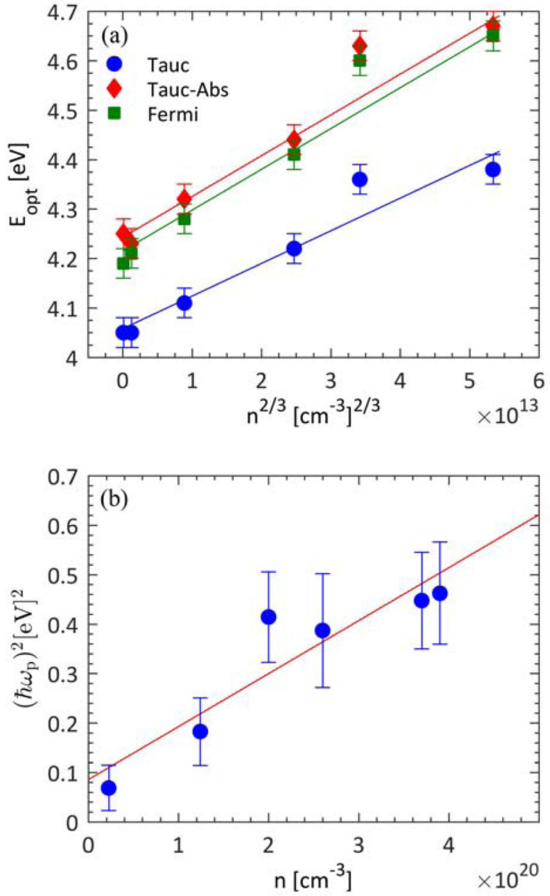

FIG. 8. (a) Optical band gap of Sb:SnO$_2$ films with increasing carrier concentration obtained using Tauc plots, combined Tauc-absorption coefficient plots, and Fermi-Dirac fits of the absorption edge, and the corresponding fits to Eq. (3). (b) Plasma frequency versus carrier concentration and the corresponding fit to Eq. (1).

The value of m_c^* obtained from the variation in plasma frequency with n is close to that reported in previous computational [7,25,64] (0.26–0.31) m_e and experimental [7,16,65] (0.1–0.39) m_e studies, whereas the higher value of m_d^* is in agreement with previous values reported for chemical vapor deposition (CVD) [61], spray pyrolysis [16], and radio-frequency (RF) reactive sputtered [66] SnO$_2$ films (of 0.59, 0.73, and 0.46) m_e, respectively. The physical origin of this higher value of m_d^* may be due to many body electron-electron interactions that become more significant as n increases and that have been shown to influence the dispersion of the conduction and valence bands [60,61].

IV. SUMMARY AND CONCLUSIONS

The PAMBE growth of epitaxial (101) SnO$_2$ films on r-plane sapphire was optimized to produce insulating material ($\rho > 1\,\mathrm{k}\Omega\,\mathrm{cm}$, $n < 10^{14}\,\mathrm{cm}^{-3}$) with an intrinsic optical band gap of (4.03 ± 0.03) eV at 300 K, that was characterized by highly crystalline, atomically abrupt surfaces with the majority of electrically active intrinsic defects contained in the first five atomic layers adjacent to the substrate. This intrinsic-quality material was then used to explore the conductivity and transparency limits of Sb doped SnO$_2$. The electrical conductivity could be controlled over at least seven orders of magnitude by Sb-doping, covering the insulating, semiconducting, and semimetallic regimes, with a maximum conductivity limit observed at $\rho \approx 6 \times 10^{-4}\,\Omega\,\mathrm{cm}$ and $n \approx 4 \times 10^{20}\,\mathrm{cm}^{-3}$, corresponding to a Sb concentration of 3×10^{20} atoms/cm^3. Any further increase in Sb flux past this limit resulted in a decrease in conductivity, most likely due to charge compensation resulting from the preferential formation of Sb^{3+} acceptors. No significant deterioration of the crystalline quality of the Sb:SnO$_2$ films with increasing Sb incorporation was observed in either RHEED or XRD analysis, indicating that the conductivity limit is likely to be determined by changes in the electronic nature of incorporated Sb species. The observed conductivity limit therefore coincides with the Fermi level position at which the donor-like (Sb^{5+}) and acceptor-like (Sb^{3+}) states of antimony have the same formation energy, i.e., the charge neutrality level of SnO$_2$.

The limits for the coexistence of high transparency and electrical conductivity were found to be determined by a BM shift of up to 0.49 eV in the optical band gap in the UV region (from 310 to 280 nm) and by a much larger blue shift (from beyond 14 to less than 2 μm) in the free-carrier adsorption edge in the IR region, due to an increased plasma frequency. Both these effects scaled with the carrier concentration of the material, reaching a maximum at the conductivity limit of $n \approx 4 \times 10^{20}\,\mathrm{cm}^{-3}$. This correlation allowed an estimated experimental value of $E_C + (0.49 \pm 0.08)$ eV to be proposed for the charge neutrality level of SnO$_2$, which is very close to the predicted theoretical value from first principles calculations. Remarkably, the transparency in the visible region was almost unchanged, with more than 90% transmission in the 300–1500 nm range for 150-nm-thick Sb:SnO$_2$ films at the conductivity limit, suggesting considerable promise for the use of Sb:SnO$_2$ materials in transparent electronics.

ACKNOWLEDGMENTS

This work was financially supported by the University of Canterbury, the MacDiarmid Institute for Advanced Materials and Nanotechnology, and the Royal Society of New Zealand Rutherford Discovery Fellowship Scheme. Aspects of this research were undertaken on the Soft X-ray Spectroscopy beamline at the Australian Synchrotron, part of ANSTO. We gratefully acknowledge expert assistance from beamline scientists B. Cowie, L. Thomsen, and A. Tadich.

---

[1] C. J. Traverse, R. Pandey, M. C. Barr, and R. R. Lunt, Nat. Energy **2**, 849 (2017).

[2] J. C. Goldschmidt, Nat. Mater. **17**, 218 (2018).

[3] J. Ronge, T. Bosserez, D. Martel, C. Nervi, L. Boarino, F. Taulelle, G. Decher, S. Bordiga, and J. A. Martens, Chem. Soc. Rev. **43**, 7963 (2014).

[4] A. N. Banerjee and K. K. Chattopadhyay, Prog. Cryst. Growth Ch. **50**, 52 (2005).

[5] A. Jerger, H. Kohler, F. Becker, H. B. Keller, and R. Seifert, Sensor. Actuat. B-Chem. **81**, 301 (2002).

[6] H. Kohler, J. Rober, N. Link, and I. Bouzid, Sensor. Actuat. B-Chem. **61**, 163 (1999).

[7] M. Batzill and U. Diebold, Prog. Surf. Sci. **79**, 47 (2005).

[8] C. Kilic and A. Zunger, Phys. Rev. Lett. **88**, 095501 (2002).

[9] A. K. Singh, A. Janotti, M. Scheffler, and C. G. Van de Walle, Phys. Rev. Lett. **101**, 055502 (2008).

[10] P. Agoston, K. Albe, R. M. Nieminen, and M. J. Puska, Phys. Rev. Lett. **103**, 245501 (2009).

[11] S. Lany and A. Zunger, Phys. Rev. Lett. **106**, 069601 (2011).

[12] K. G. Godinho, A. Walsh, and G. W. Watson, J. Phys. Chem. C **113**, 439 (2009).

[13] P. D. King and T. D. Veal, J. Phys.: Condens. Matter **23**, 334214 (2011).

[14] P. D. C. King, R. L. Lichti, Y. G. Celebi, J. M. Gil, R. C. Vilão, H. V. Alberto, J. Piroto Duarte, D. J. Payne, R. G. Egdell, I. McKenzie, C. F. McConville, S. F. J. Cox, and T. D. Veal, Phys. Rev. B **80**, 081201(R) (2009).

[15] M. Batzill, J. M. Burst, and U. Diebold, Thin Solid Films **484**, 132 (2005).

[16] E. Shanthi, V. Dutta, A. Banerjee, and K. L. Chopra, J. Appl. Phys. **51**, 6243 (1980).

[17] M. E. White, O. Bierwagen, M. Y. Tsai, and J. S. Speck, J. Appl. Phys. **106**, 093704 (2009).

[18] K. C. Mishra, K. H. Johnson, and P. C. Schmidt, Phys. Rev. B **51**, 13972 (1995).

[19] H. S. So, J. W. Park, D. H. Jung, K. H. Ko, and H. Lee, J. Appl. Phys. **118**, 085303 (2015).

[20] J. E. N. Swallow, B. A. D. Williamson, T. J. Whittles, M. Birkett, T. J. Featherstone, N. H. Peng, A. Abbott, M. Farnworth, K. J. Cheetham, P. Warren, D. O. Scanlon, V. R. Dhanak, and T. D. Veal, Adv. Funct. Mater. **28**, 1701900 (2018).

[21] D. D. Purkayastha, M. G. Krishna, and V. Madhurima, Mater. Lett. **124**, 21 (2014).

[22] S. Mihaiu, I. Atkinson, M. Gartner, M. Anastasescu, E. Manea, and M. Zaharescu, Proc. SPIE **8411**, 84111R (2012).

[23] M. E. White, M. Y. Tsai, F. Wu, and J. S. Speck, J. Vac. Sci. Technol. A **26**, 1300 (2008).

[24] M. A. Mäki-Jaskari and T. T. Rantala, Phys. Rev. B **64**, 075407 (2001).

[25] Y. Mi, H. Odaka, and S. Iwata, Jpn. J. Appl. Phys. **38**, 3453 (1999).

[26] F. Atay, V. Bilgin, I. Akyuz, E. Ketenci, and S. Kose, J. Non-Cryst. Solids **356**, 2192 (2010).

[27] L. Dua and P. K. Biswas, Chem. Phys. Lett. **572**, 66 (2013).

[28] M. Feneberg, C. Lidig, K. Lange, R. Goldhahn, M. D. Neumann, N. Esser, O. Bierwagen, M. E. White, M. Y. Tsai, and J. S. Speck, Appl. Phys. Lett. **104**, 231106 (2014).

[29] W. Spence, J. Appl. Phys. **38**, 3767 (1967).

[30] F. Sabino, L. Oliveira, S.-H. Wei, and J. Da Silva, J. Phys.: Condens. Matter **29**, 085501 (2017).

[31] R. Alvarez, J. C. Gonzalez, J. P. Espinos, A. R. Gonzalez-Elipe, A. Cueva, and F. Villuendas, Appl. Surf. Sci. **268**, 507 (2013).

[32] H. Y. Liu, V. Avrutin, N. Izyumskaya, U. Ozgur, and H. Morkoc, Superlatt. Microstruct. **48**, 458 (2010).

[33] P. Shusheng and L. Guanghai, Recent Pat. Nanotechnol. **5**, 138 (2011).

[34] E. Elangovan, S. A. Shivashankar, and K. Ramamurthi, J. Cryst. Growth **276**, 215 (2005).

[35] X. Feng, J. Ma, F. Yang, F. Ji, F. Zong, C. Luan, and H. Ma, Mater. Lett. **62**, 1779 (2008).

[36] M. Y. Tsai, M. E. White, and J. S. Speck, J. Cryst. Growth **310**, 4256 (2008).

[37] M.-Y. Tsai, O. Bierwagen, and J. S. Speck, Thin Solid Films **605**, 186 (2016).

[38] J. R. Arthur, Surf. Sci. **500**, 189 (2002).

[39] A. Y. Cho and J. R. Arthur, Prog. Solid State Chem. **10**, 157 (1975).

[40] L. B. Freund and S. Suresh, *Thin Film Materials: Stress, Defect Formation and Surface Evolution* (Cambridge University Press, New York, 2004).

[41] See Supplemental Material at http://link.aps.org/supplemental/10.1103/PhysRevB.98.155308 for details on the optimization of the growth conditions and for further characterization studies.

[42] M. J. Wahila, K. T. Butler, Z. W. Lebens-Higgins, C. H. Hendon, A. S. Nandur, R. E. Treharne, N. F. Quackenbush, S. Sallis, K. Mason, H. Paik, D. G. Schlom, J. C. Woicik, J. Guo, D. A. Arena, B. E. White, G. W. Watson, A. Walsh, and L. F. J. Piper, Chem. Mater. **28**, 4706 (2016).

[43] R. G. Egdell, J. Rebane, T. J. Walker, and D. S. L. Law, Phys. Rev. B **59**, 1792 (1999).

[44] R. G. Egdell, T. J. Walker, and G. Beamson, J. Electron. Spectrosc. **128**, 59 (2003).

[45] P. M. A. Sherwood, Phys. Rev. B **41**, 10151 (1990).

[46] J.-M. Themlin, M. Chtaïb, L. Henrard, P. Lambin, J. Darville, and J.-M. Gilles, Phys. Rev. B **46**, 2460 (1992).

[47] M. A. Stranick and A. Moskwa, Surf. Sci. Spectra **2**, 50 (1993).

[48] M. A. Stranick and A. Moskwa, Surf. Sci. Spectra **2**, 45 (1993).

[49] J. M. Themlin, R. Sporken, J. Darville, R. Caudano, J. M. Gilles, and R. L. Johnson, Phys. Rev. B **42**, 11914 (1990).

[50] M. Feneberg, C. Lidig, K. Lange, M. E. White, M. Y. Tsai, J. S. Speck, O. Bierwagen, and R. Goldhahn, Phys. Status Solidi A **211**, 82 (2014).

[51] J. Fayat and M. S. Castro, J. Eur. Ceram. Soc. **23**, 1585 (2003).

[52] C. N. Luan, Z. Zhu, W. Mi, and J. Ma, J. Alloys Compd. **586**, 426 (2014).

[53] I. S. Mulla, H. S. Soni, V. J. Rao, and A. P. B. Sinha, J. Mater. Sci. **21**, 1280 (1986).

[54] J. F. Moulder and J. Chastain, *Handbook of X-ray Photoelectron Spectroscopy: A Reference Book of Standard Spectra for Identification and Interpretation of XPS Data* (Physical Electronics Division, Perkin-Elmer Corporation, Waltham, Massachusetts, 1992).

[55] A. R. McNeill, K. J. Bell, A. R. Hyndman, R. M. Gazoni, R. J. Reeves, A. J. Downard, and M. W. Allen, J. Phys. Chem. C **122**, 12681 (2018).

[56] C. Terrier, J. P. Chatelon, R. Berjoan, and J. A. Roger, Thin Solid Films **263**, 37 (1995).

[57] A. Dolgonos, T. O. Mason, and K. R. Poeppelmeier, J. Solid State Chem. **240**, 43 (2016).

[58] B. Falabretti and J. Robertson, J. Appl. Phys. **102**, 123703 (2007).

[59] J. Robertson and S. J. Clark, Phys. Rev. B **83**, 075205 (2011).

[60] K. F. Berggren and B. E. Sernelius, Phys. Rev. B **24**, 1971 (1981).

[61] G. Sanon, R. Rup, and A. Mansingh, Phys. Rev. B **44**, 5672 (1991).

[62] S. K. Vasheghani Farahani, T. D. Veal, J. J. Mudd, D. O. Scanlon, G. W. Watson, O. Bierwagen, M. E. White, J. S. Speck, and C. F. McConville, Phys. Rev. B **90**, 155413 (2014).

[63] H. Fujiwara and M. Kondo, Phys. Rev. B **71**, 075109 (2005).

[64] M. Batzill, K. Katsiev, J. M. Burst, U. Diebold, A. M. Chaka, and B. Delley, Phys. Rev. B **72**, 165414 (2005).

[65] C. G. Fonstad, J. Appl. Phys. **42**, 2911 (1971).

[66] N. Miyata and H. Kitahata, Thin Solid Films **125**, 33 (1985).